A combined wind and wave energy-converter concept in survival mode: numerical and experimental study in regular waves with a focus on water entry and exit

Ling Wan[1,2], Marilena Greco[1,2,3,4], Claudio Lugni[1,2,3,4], Zhen Gao[1,2,3], Torgeir Moan[1,2,3]

1. *Centre for Ship and Ocean Structures (CeSOS)*
2. *Department of Marine Technology, Norwegian University of Science and Technology (NTNU) Trondheim, Norway*
3. *Centre for Autonomous Marine Operations and Systems (AMOS)*
4. *Marine Technology Institute, National Research Council, CNR-INSEAN, Rome, Italy*

Abstract

Water entry (including slamming) and exit phenomena as well as green water on deck were observed during survivability model tests of a combined wind and wave energy converter concept. Here, a nonlinear numerical model based on a blended station-keeping potential-flow solver with a local impact solution for bottom slamming events and an approximated model for the water shipped on the deck is proposed to simulate these nonlinear phenomena. Viscous damping loads are modelled through empirical formulas. The comparisons between the numerical model and model tests are globally satisfactory in terms of platform motions, mooring-line tensions, and occurrence and features of water-entry, water-exit and water on deck events. The results show that, in almost all examined cases, the slamming starts from the center of the torus bottom, the water shipping occurs almost contemporary from the wave and lee side of the deck. In the shortest examined waves both phenomena start from the wave side. From the investigation, the water on deck is very effective in reducing the double wave frequency (2ω) component of the surge, heave and pitch motions for sufficiently large incident-wave periods and in reducing the mean surge and pitch motions close to the heave resonance. The slamming events have a limited effect on the body motions.

Keywords: Nonlinear hydrodynamic analysis; Combined wind and wave energy converter; Water entry and exit; Slamming; Water on deck.

1. Introduction

Offshore wind technology has rapidly developed in recent years with a trend towards larger scale wind turbines, deeper water depth and larger wind farm sizes with sites further from shore. Wave energy also represents an energy resource with great potential and a much higher power density than wind power. The performance of such devices in normal operating conditions and their survivability in extreme environmental conditions must be assessed. Several in-depth researches on specific concepts have been carried or are ongoing, for example, Wei et al. (2015, 2016) investigated experimentally and numerically an oscillating wave surge converter with focus on viscous effects in normal operating conditions and slamming effects in extreme conditions. In view of investment reduction, it is beneficial for wind and wave energy converters to share infrastructure such as support structures, power substations, mooring systems and cables. Through the EU FP7 Marine Renewable Integrated Application Platform (MARINA) project (Sojo and Auer, 2014), several combined wind and wave energy converter concepts were proposed to address the integration of wind and wave energy devices on a single platform with the focus on floating concepts for deep water application: the spar-torus combination (STC) concept; the semi-submersible flap concept (SFC) and the oscillating water column (OWC) array with a wind turbine installed. The SFC (Luan et al., 2014; Michailides et al., 2014) incorporates a 5 MW semi-submersible floating wind turbine with three flap-type WECs installed on the three pontoons of the floater. Functionality and survivability model tests of the SFC with a 1:50 scale ratio have been performed in the ocean basin at Ecole Centrale De Nantes (ECN), France (Michailides et al., 2015; Michailides et al., 2016). The OWC array platform has been proposed by the Hydraulics and Maritime Research Centre in University College Cork (HMRC/UCC). The OWC arrays include 20 OWC chambers with 10 OWCs installed in each arm facing the main wave direction, and a wind turbine is installed on top of the structure. The STC concept is the focus of present study.

As shown in the plot (a) in Figure 1, the STC concept is composed of a 5MW spar floating wind turbine and a torus-shaped wave energy converter (WEC). The torus can move along the spar floater to absorb wave energy. Power take off (PTO) system is installed between spar and torus, and a delta shaped catenary mooring system is deployed in the STC prototype. In addition, several survival strategies were proposed (Muliawan et al., 2013) to ensure the survivability of the concept in severe sea states (Hs>6m). Ongoing research investigation is aimed to examine and assess both the functionality and survivability of the STC concept numerically and experimentally. In the first phase, operational conditions (Hs<6m) were studied experimentally and numerically using a linear potential-flow solver and are documented by Wan et al. (2016a). In the second phase, two of the survival strategies proposed (Muliawan et al., 2013) were investigated numerically and experimentally (Wan et al., 2015). In the Mean Water Level (MWL) survival mode (left part of Figure 1 (b) and middle of Figure 2), the torus is locked on the spar floater and floats at the mean water level position. In the submerged (SUB) mode (right part of Figure 1 (b) and right of Figure 2), the torus is locked on the spar floater and then fully submerged to a specified position by additional ballast in the spar bottom.

The numerical method for the two investigation phases used is based on the hybrid frequency and time domain method (Naess and Moan, 2013): the linear hydrodynamic properties are obtained based on a linear potential flow solver in frequency domain and then transferred to time domain through retardation functions, and the hydrodynamic excitation forces are pre-generated linearly in the time domain. The nonlinear viscous forces, power take off forces, mooring line forces, interface forces etc. are also considered. The time domain model was generated in SIMO (SImulations of Marine Operations) code (MARINTEK, 2007), which was developed by MARINTEK and can be used to perform motion analysis of multi-body under wave, wind and current loads. In the cases without strongly nonlinear phenomena, i.e. water entry and exit (WEE) of the torus in the functionality and survivability model tests, the numerical model based on the linear potential flow solver provides good results compared with model tests (Wan et al., 2015; Wan et al., 2016a). However, under the MWL survival mode in the survivability model test, WEE of torus were observed. For these cases, this numerical model was not able to provide reliable results compared with model tests (Wan et al., 2015).

To capture the strongly nonlinear phenomena in the MWL survivability model test, a numerical model based on a three-dimensional nonlinear sea-keeping numerical solver, combined with a local analytical solution for the slamming loads and a nonlinear shallow-water model for water shipping events is used in the present work. The focus is on regular wave test cases and all the results in this paper are presented in full scale or non-dimensional values unless otherwise specified. Preliminary validation studies of the numerical method are documented by Wan et al. (2016b).

The paper is organized as follows. First, the experimental set-up is briefly outlined and the typical features of the nonlinear phenomena observed in the tests are documented. An uncertainty analysis of the tests is also carried out. In section 3, the numerical method is described and, in section 4, it is validated against the model tests. At the same time, a physical investigation of the occurrences and features of water entry and exit phases accompanied by water on deck and slamming is performed using the two research methods. The last section draws the main conclusion and future work.

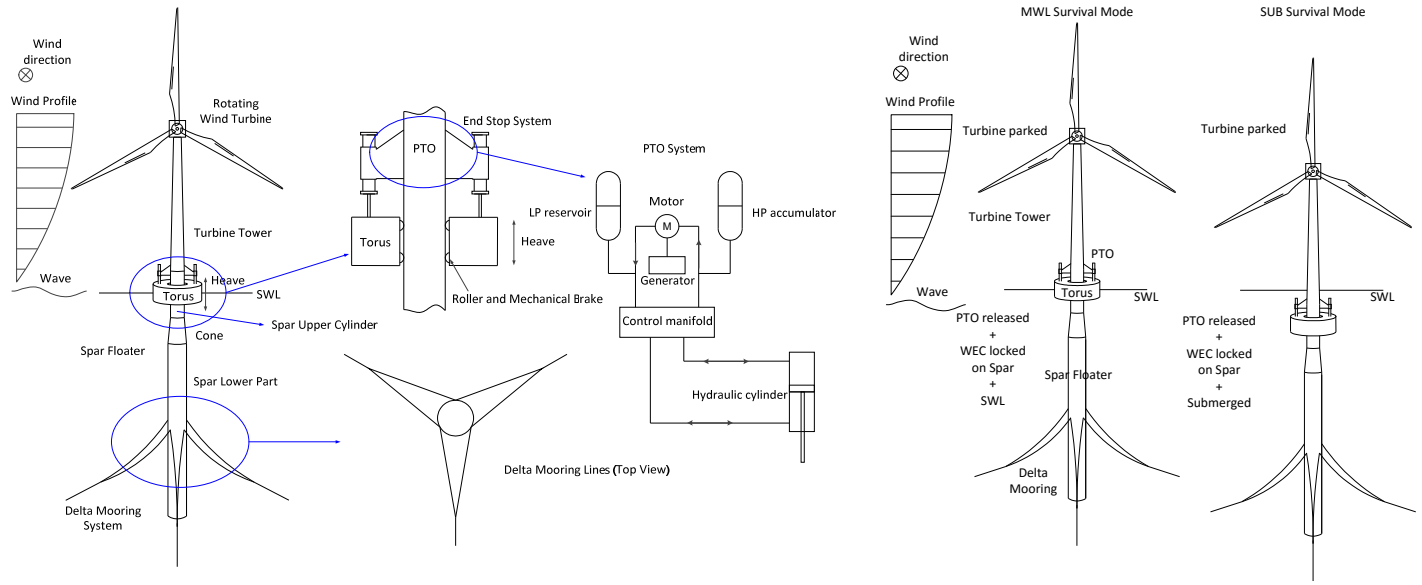

(a) (b)

Figure 1. STC concept and the MWL and SUB survival modes.

2. Model tests

The model tests with focus on the survivability were performed in the towing tank of MARINTEK, Norway. The dimensions of the towing tank are length=260 m, breadth=10.5 m, and water depth=10/5.6 m (MARINTEK, 2014). In particular, the depth is 10 m from the wave maker over a 85m distance, and is 5.6 m in the other part of the tank. Froude scaling was followed, and the scaling ratio is 1:50. The STC concept and the physical model under the MWL survival mode in the tests are shown in Figure 1 (a) and (b), where the inertial coordinate system used is also shown. This system is set as follows: z-direction is positive upwards, x-direction is positive in the wave-maker direction, and the y-direction follows the right-hand rule. The origin is at the intersection between the still water surface and the vertical axis of the spar at rest.

2.1 Experimental set up

The physical model was placed in the tank region with 10 m water depth. Relevant aspects of the experimental set-up in the survivability model tests and the two survival modes of the platform, i.e., MWL mode and SUB mode, are shown in Figure 2. The plan view of the model test layout is provided in Figure 3. The dimensions of the STC components are presented in Table 1. In the model tests, wave elevations, 6 degree of freedom (D.O.F) body motions, interface forces between the spar and the torus, and mooring-line tensions were measured. The global features of the wave-body interactions in the experiments were recorded with a low-speed camera with 50 fps.

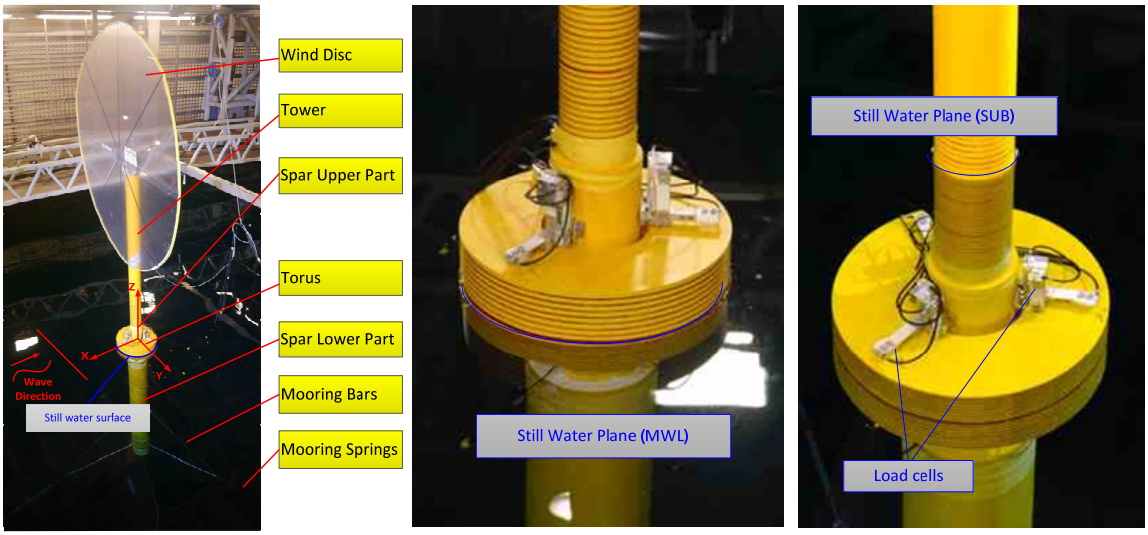

Figure 2. Physical model in the survivability model test, different components and the MWL and SUB survival modes

The motions of the model were measured using the Qualisis optical system and were tracked by three reflection balls and eight cameras. The reflection balls were installed on top of the tower. Four resistance-type wave probes were used in the tests as shown in Figure 3. Eighteen HBM DF-2S water proof bending load cells were combined and installed to fix the torus onto the spar, and to measure the relative forces between spar and torus with sampling frequency 2400 Hz. These forces are named interface forces in this paper. For a single load cell, the nonlinearity, the hysteresis error and the creep over 5 mins are all between -0.05% to +0.05% of the sensitivity. A body-fixed coordinate system is used when the spar-torus interface forces are measured. This is coincident with the inertial coordinate system when the body is at rest in calm water condition, and moves with the body in waves. Horizontal and vertical interface forces Fx and Fz along the local x and z directions, respectively, are investigated. The mooring-line system was simplified as three rigid bars to represent the delta lines, connected by three linear springs to represent the catenary line. The mooring points are shown in Figure 3. The first mooring point is located in front of the model in the wave maker direction, and the other two points are located behind of the model in the wave travelling direction. The mooring-line tensions are denoted as F_{MLF} (Front), F_{MLL} (Left), and F_{MLR} (Right), respectively. The pretensions are 1250 kN. Mooring-lines stiffness for F_{MLF}, F_{MLL} and F_{MLR} are 54.5 kN/m, 65.75 kN/m, and 65.75 kN/m, respectively. All the control and electronic devices, e.g., computers for recording data, control system of the wave maker, wind generation, carriage position, and video cameras, as well as the A/D converters and the channel amplifiers are located on the control platform.

Table 1. STC dimensions.

Spar and Tower		[m]
Lower part of spar	Diameter	10
	Length	108
Upper part of spar	Diameter	6.45
	Length	24
Tower	Diameter	5.5
	Length	77
Total weight		8891.25 [ton]
Torus		[m]
	Height	8
	Outer diameter	20
	Inner diameter	8
	Weight	1145 [ton]

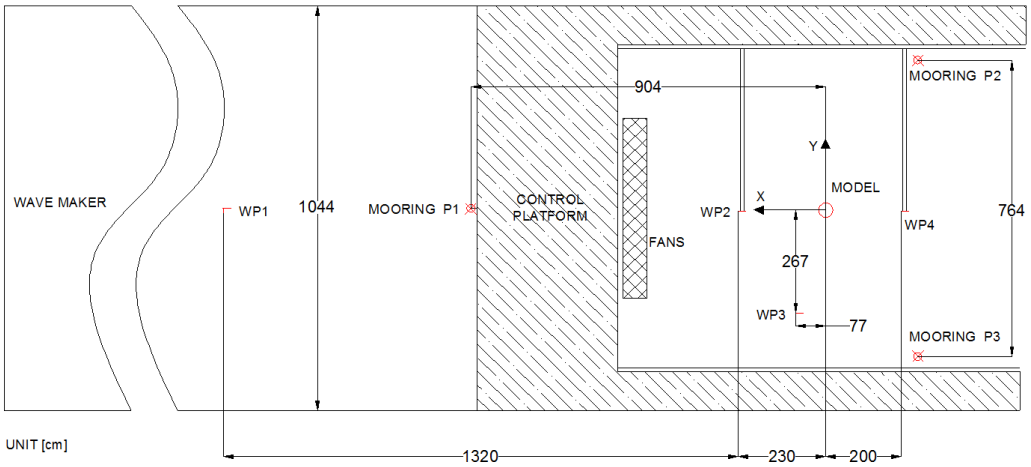

Figure 3. Plan view of the model test layout

Decay tests, regular and irregular wave tests and wind tests both in MWL and SUB survival modes were carried out. In this paper, only the regular wave test cases of the MWL survival mode are examined.

The natural periods of the MWL mode for the first five degrees of freedom of the moored platform were identified from free-decay tests and are shown in Table 2. The yaw motion would be zero for the bare platform due to its radial symmetry and is expected to be small for the used experimental set-up.

Table 2. Natural periods for the STC in MWL mode as identified from free decay tests.

	(η_1)	(η_2)	(η_3)	(η_4)	(η_5)
T [s]	98	93	13	36	37

In the regular-wave tests, two wave heights were considered, i.e. H=2m and H=9m, while the wave period T covered a range from 9 s to 23 s. The regular wave test matrix is presented in Table 3.

Table 3. Regular wave test matrix and the occurrence of the strong nonlinear phenomena

Test mode	T[s] / H[m]	9	11	12	13	14	15	17	19	21	23
MWL	2										
	9	Water entry and exit									

For the MWL mode, different nonlinear phenomena have been observed for incident-wave periods within the resonance region of heave motion: water entry and exit (WEE) phases and water on deck (WOD). The interface-force measurements highlighted the occurrence of slamming (SLAM) during the initial stages of water-entry events through appearance of peaked behavior followed by high-frequency oscillations. For longer incident-wave periods examined experimentally, the platform experienced parametric-pitch resonance. In the following, we focus on the occurrence and features of WEE, SLAM and WOD phenomena and on their relevance for the motions and response of the platform.

2.2 Physical investigation of water entry and exit phenomena in the model tests

The water entry and exit phenomena observed in the regular-wave tests are highlighted with colored background in Table 3. Important WOD events occurred in the same range of periods for the largest wave height, while no water shipping or negligible amount of water reached the torus deck for H=2 m. From the features of the measured interface-force components, the slamming events were also associated only with H=9 m.

Snapshots of the WEE from the video recorded in the tests for the incident waves with H=9m and T=15s are shown in Figure 4. The non-dimensional time series of the heave, pitch and relative vertical motion for the three test cases with H=9m, and T=11s, 13s and 15s are presented in the bottom plots of Figure 5. The upper and lower horizontal lines in the plots represent the freeboard (f_{torus}) and bottom (opposite of the draft h_{torus}) torus, respectively. The top plots of Figure 5

provide the corresponding non-dimensional interface forces in the local x and z directions, i.e. Fx and Fz. The four vertical dashed lines in the left plots refer to the time instants of the snapshots in Figure 4. All the parameters are presented in non-dimensional form: the time t is divided by the wave period T; the translational motions are divided by the incident-wave amplitude ζ_a = H/2; the rotational motions are divided by the incident-wave steepness $k\zeta_a$, where $k=2\pi/\lambda$ is the wave number and λ is the wave length. The force parameters are divided by ρgV, where ρ is the density of water, g is the gravitational acceleration and V is the submerged volume of the torus. The relative vertical motion analyzed here is defined as $s_r = \zeta_0 - \eta_3$, where ζ_0 is the instantaneous undisturbed wave elevation estimated at the origin of the coordinate system and η_3 is the measured heave motion of the torus. This means that (a) radiated and diffracted waves are not considered because they were not measured and (b) the effects of surge and pitch motions are neglected. It implies that local error exists between s_r and the relative vertical motion between the local wave elevation and the body motions. However, this error should be limited in the cases examined. By considering that the wave length $\lambda >> D_{torus}$, where D_{torus} is the torus outer diameter, and considering that the surge motion at the still water line (SWL) is small enough compared with λ, one can generally assess whether the torus is out of water or totally submerged into water by comparing the approximated relative vertical motion s_r with the torus draft and with the freeboard, respectively.

The WEE process is characterized by four main stages which are labelled from ‘a’ to ‘d’ in Figure 4 and the left plot of Figure 5. The snapshot labelled as ‘a’ in Figure 4 shows the beginning of a wave entry event. At this stage, s_r equals the torus bottom and is increasing. The torus is going downward, i.e., the heave is decreasing, and the pitch motion is negative, i.e. wave-side upwards, so the lee-side of the torus is the first one entering the water. The water entry phase at this time instant induces high-frequency content and relevant peaks on the interface forces. This suggests the occurrence of a slamming event.

Successively, the torus continues going down until time instant ‘b’, when the water reaches the torus top and invades the deck, i.e. s_r equals the torus freeboard and continues increasing. This corresponds to the start of a WOD event. Between instants ‘b’ and ‘c’ the torus is fully submerged, the maximum amount of water shipped occurs at the maximum of the relative vertical motion. Because of the phase shift between heave, pitch and the instantaneous wave elevation (not shown here), the time instant with maximum amount of water shipping t_M is not coincident with that of the minimum absolute vertical motion, i.e. of the minimum heave motion in our approximation. After t_M, the torus goes upwards until time instant ‘c’. The time instant ‘c’ corresponds to the stage that the torus top is going out of water, i.e., s_r equals the torus freeboard and is decreasing.

From time instant ‘c’ to ‘d’, s_r decreases until the torus draft is reached. At the time instant ‘d’, the torus is totally out of water. After that, gravity forces are dominant on the torus, which can be observed from the vertical interface force Fz, because the ratio between Fz and the torus weight is approximately 1. After the time instant ‘d’, s_r reaches the minimum value and then increases until the torus bottom, when a new water-entry event with slamming starts (last snapshot labelled as ‘a’ in Figure 4).

Figure 4. Strongly nonlinear phenomena in the model test for incident waves with H=9m and T=15s: water entry (a and b), green water (b and c) and water exit (c and d). Time increases from left to right.

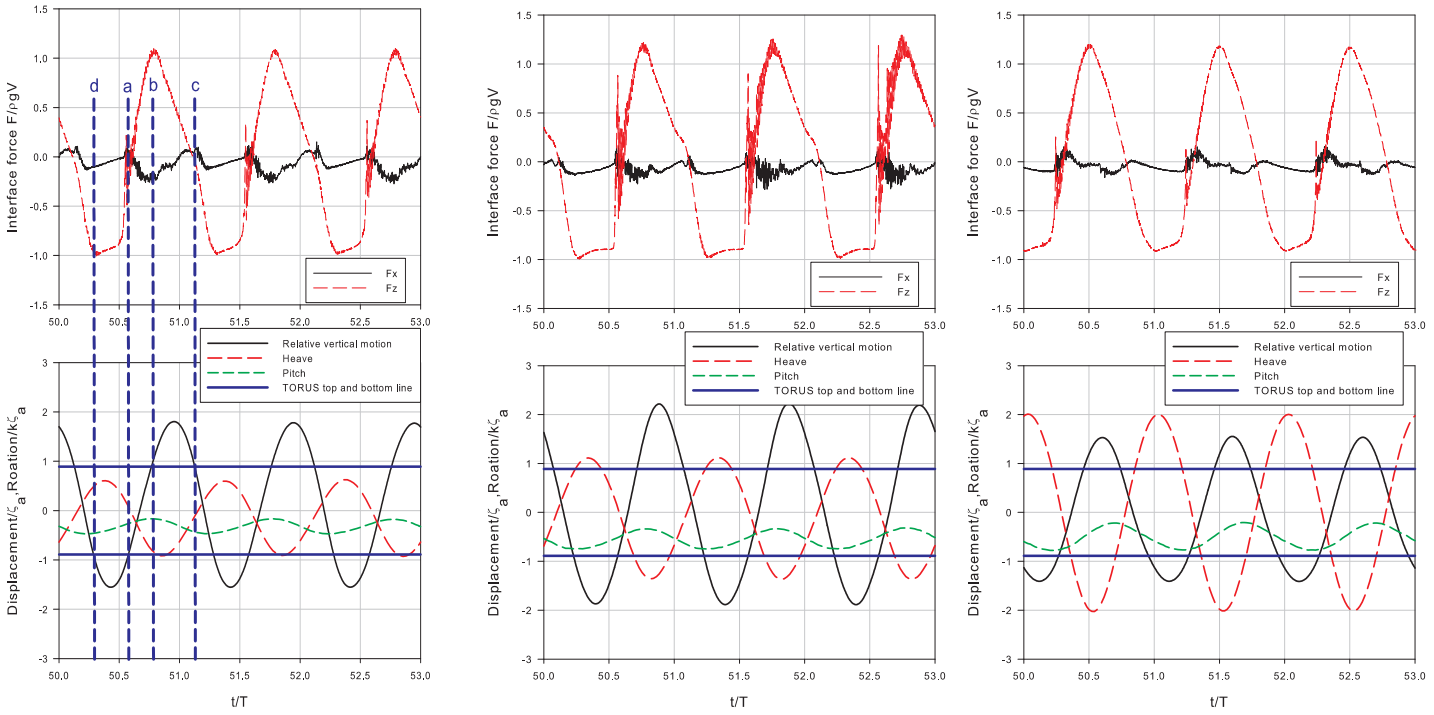

Figure 5. Physical investigation of motions and interface forces from three different test cases with H=9m and T=11s (left), T=13s (middle) and T=15s (right), respectively. The vertical dashed lines indicate the time instants of the snapshots shown in Figure 4.

In this WEE, SLAM and WOD process, the interface forces are strongly influenced by the nonlinear hydrodynamic forces induced by the incident waves on the STC concept, while the motion responses are not significantly affected. In Figure 5, it is clear that the curves of Fz have different slamming peaks under different cases, largest peaks are observed in the case with T=13s, where the relative vertical motion reaches also the maximum values, while the amplitude of the heave motion is largest in the case with T=15s. This indicates that the heave motion amplitude is not the only parameter affecting the slamming peaks, because also relative phases between the different motions and the wave elevation matter. In particular, the larger amplitude of s_r, combined with relatively similar wave frequency among the three cases, suggests a larger relative vertical velocity, between the waves and the body, for T=13s. This, together with the impact angle, is an important parameter for the occurrence of a slamming event during water entry and for its severity.

2.3 Uncertainty analysis of the experiments

The uncertainty analysis is a critical part in the model tests, and gives an indication of the results reliability. The random error during the experiments is quantified in this part. More uncertainty analysis results of the model tests for cases without strongly nonlinear phenomena can be found in Wan et al. (2015).

The regular wave test case with H=9m and T=12s is studied for the random error estimation. A total number of 40 cycles of the steady-state regular time series are analyzed. The time window with two regular cycles is used in each estimation, so 20 estimations were performed. At every time instant, the mean and standard deviation (STD) considering all the time windows are calculated. The mean and slow drift values for the motions are eliminated.

The time series of non-dimensional wave elevations, surge and heave motions, as well as the vertical interface force Fz are investigated. The mean values and random errors which are represented by STD of these time series are presented in Figure 6. The random errors are shown as error bars located in different time instants. The average values of the STDs are calculated and shown in Table 4. From the analysis, the mean STDs are below 10% for all examined variables, with largest value for the wave elevation.

Table 4. Average values of the random errors of non-dimensional time series for wave elevations, surge and heave motions, and Fz

H=9m, T=12s	Wave elevation ζ/ζ_a	Surge η_1/ζ_a	Heave η_3/ζ_a	Vetical interface force Fz/ρgV
Average values of STDs	9.2%	4.3%	6.0%	8.8%

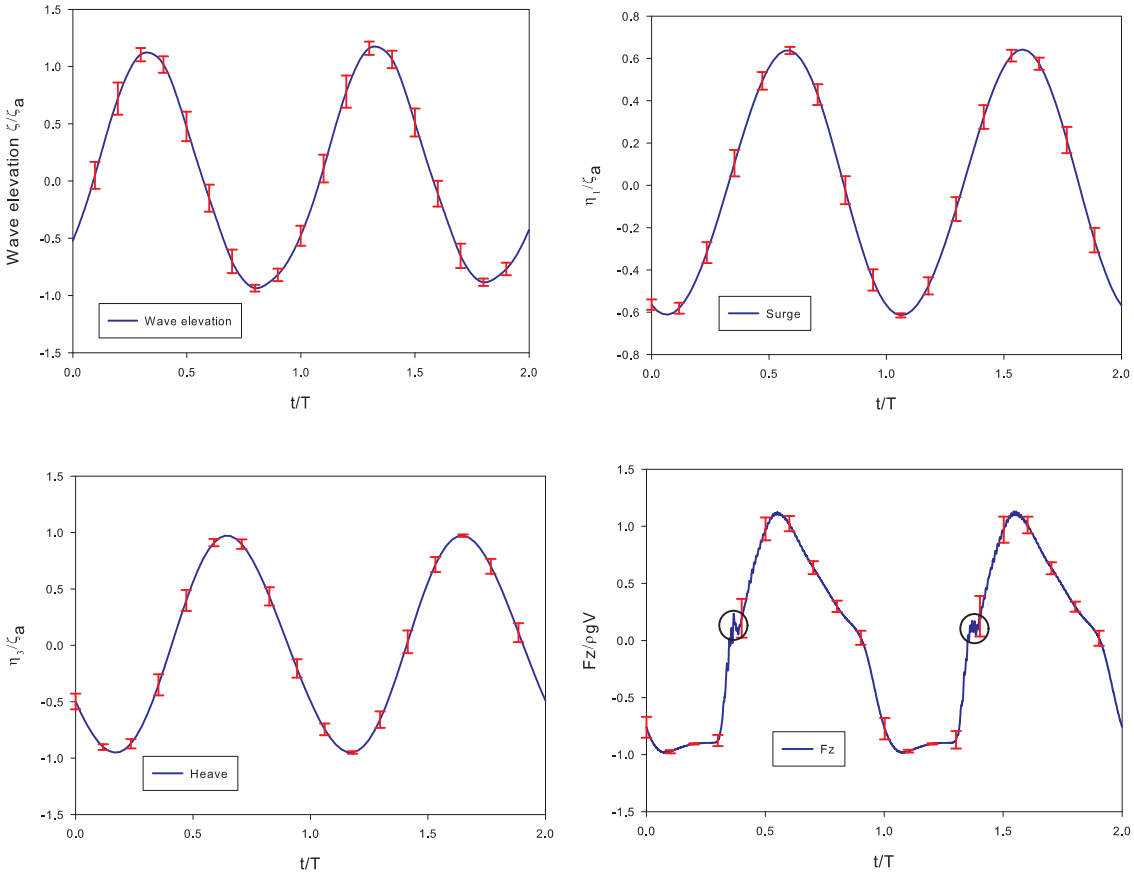

Figure 6. Mean values and random errors of the non-dimensional time series for wave elevations, surge and heave motions, and vertical interface force Fz for the case with H=9m and T=12s.

This analysis is not suitable for the peaked region of the interface-force time history occurring during the initial state of the water entry phases. The averaging process of the uncertainty analysis filters this out completely. The peaked region is indicated in the right-bottom plot of Figure 6 by a circle during each water-entry phase shown. This highlights a stochastic behavior of the peaked region of the interface force and suggests the occurrence of sufficiently blunt impacts during the experiments, leading to slamming forces with peaks of stochastic nature.

3. Nonlinear numerical modelling

A blended method based on potential-flow theory with viscous corrections for the damping loads is used to handle the dynamic behavior of the moored STC platform. The solver partially accounts for nonlinear hydrodynamic effects on the structure, in particular can handle possible occurrence of slamming and water-on-deck phenomena. The basic solver is the one proposed by Greco and Lugni (2012), successfully validated by Greco et al. (2012) for large wave-induced motions, involving slamming and water on deck, by comparing against model tests on a patrol ship. The method was able to handle parametric resonance on an FPSO without bilge-keels, when compared against related model tests; moreover, it highlighted the mutual influence between parametric roll and water on deck (Greco et al., 2014). It was extended by Greco et al. (2015) to incorporate anchor-line loads for the study of an FPSO in regular waves with generic heading and by Lugni et al. (2015) to investigate a particular parametric instability between yaw and roll motions. The detailed

description of the solver can be found in the referred works; here the main features are briefly outlined and the peculiarities with respect to the previous implementations are pointed out.

The solution algorithm is based on a Domain Decomposition (DD) strategy coupling (A) a seakeeping/station-keeping potential-flow solver with (B) a local impact solution for bottom slamming events and (C) an approximated model for the water shipped on the deck. Method (A) solves the equations of motions in time domain using the Cummins approach (Cummins, 1962). This means that the radiation loads are expressed in terms of an instantaneous contribution connected with the added-mass and damping coefficients at infinite frequency and convolution integrals connected with free-surface memory effects. This approach is necessary to study transient phases and motions involving more than one frequency and strictly speaking is valid within linear theory. In practice, its use has been stretched outside its limits of applicability and nonlinear loads, relevant for the specific examined case, are modeled individually and added in the right-hand-side of the equations of motions.

The basic DD performs a correction of the linear radiation and diffraction loads to account for weakly nonlinear effects within the weak-scatterer hypothesis for the wave-body interaction problem. This means that scattering and radiation effects are assumed small with respect to the body motions and the incident waves, and corrections of them can be obtained by enforcing averagely the impermeability condition along the instantaneous body wetted surface defined by the rigid body motions and the incident-wave elevation (Greco and Lugni, 2012). For the problem of interest, the scattering loads for surge and pitch are not small compared with the Froude-Krylov loads due to the cylindrical shape of the STC with circular cross-sections. This invalidates the weak-scatterer assumption. Therefore, the correction of the linear scattering and radiation loads associated with the weak-scatterer approach is not applied and these two loads contributions are estimated directly as linear loads.

In the present solution algorithm, the equations of motion are written in the body fixed coordinate system with origin in the point on the mean free surface with the same horizontal position as the center of mass when the STC is in its mean configuration. The x-axis is positive against the incident-wave direction, the z-axis is positive upwards and the y-axis is obtained using the right-hand rule. For the STC, the infinite-frequency damping loads coincide with infinite-frequency wave-radiation damping loads and therefore are zero. The inertia and infinite-frequency added-mass loads, connected with the body acceleration, balance the linear radiation loads, the Froude-Krylov ($\boldsymbol{F}_{FK}$) and hydrostatic ($\boldsymbol{F}_{hyd}$) loads, the mooring-line restoring ($\boldsymbol{F}_{moor}$) type of loads, the viscous damping loads ($\boldsymbol{F}_{visc}$), and the bottom-slamming ($\boldsymbol{F}_{slam}$) and water-on-deck ($\boldsymbol{F}_{wod}$) loads. Nonlinear $\boldsymbol{F}_{FK}$ and $\boldsymbol{F}_{hyd}$ are estimated integrating the related pressure term along the instantaneous wetted-surface of the platform (with upper limit the torus freeboard) defined by the rigid body motions and the incident-wave elevation accurate to the second order. The forces and moments coming from $\boldsymbol{F}_{FK}$ and $\boldsymbol{F}_{hyd}$ are directly estimated in the body-fixed reference frame.

The cables system described in section 2.1 is explicitly modeled in the solver and the resulting loads are estimated assuming linear restoring effects from the cables. More in detail, the moving nodes follow the rigid motions of the platforms; this provides the instantaneous configuration of the cables and the length variation of each mooring line, say ΔL. The related tension is estimated as $AE \cdot \Delta L$ and is directed along the mooring line. The forces from the mooring lines are projected along the axes of the body-fixed reference frame and the related moments are estimated as torques of forces applied at the cable nodes fixed to the body.

The viscous damping loads from the torus, the spar and the six steel bars composing the delta-mooring system used in the experimental set-up are estimated using available empirical formulas (Faltinsen, 1993), while the contribution from the three mooring-lines is assumed negligible. In particular, the cross-flow principle is applied along the spar, the torus and the six bars to find the 3D drag force contributions, acting normally to the axis of each of these cylindrical components, as integration of the drag force per unit length formally given as

$$\boldsymbol{F}'_{drag,h} = \frac{1}{2}\rho D_{kc} C_D \boldsymbol{u}_{rel} \left|\boldsymbol{u}_{rel}\right| \tag{1}$$

with ρ the water density, D_{kc} and C_D, respectively, the diameter and drag coefficient of the cross-section and $\boldsymbol{u}_{rel}$ the projection vector in the cross-section plane of the relative velocity between the incident wave and the platform at the center of the cross-section. For the spar and the torus, the drag coefficient C_D depends in general on the local Keulegan-Carpenter (KC) number and is estimated as follows

$$C_D = \begin{cases} C_{D1} = \dfrac{3\pi^3}{2KC}[(\pi\beta)^{-1/2} + (\pi\beta)^{-1} - \dfrac{1}{4}(\pi\beta)^{-3/2}] & \text{for } KC < KC_0 \qquad (\beta = D_{kc}^{\,2}/\nu T_{kc}) \\ C_{D2} = 0.2KC & \text{for } KC_0 < KC < 10 \\ C_{D3} = 1.2[1 + 0.58e^{-0.064KC}]^2 & \text{for } KC > 10 \end{cases}$$

Here, ν is the kinematic viscosity coefficient and T_{kc} is the characteristic period of oscillation. In waves, T_{kc} is set equal to the incident-wave period while in free-decay tests it is set equal to the natural period of the involved degree of freedom. The KC number is estimated as $KC = U_{kc}T_{kc}/D_{kc}$, with U_{kc} the amplitude of relative velocity between the incident waves and the body locally at the cross-section in a period T_{kc}. It means that KC is in general different for each cross-section and can change in time during a transient phase. KC_0 fixes the passage from C_{D1} for non-separated flow (Wang, 1968) to C_{D2} for separated flow (Bearman et al., 1984) and is chosen as 1.8 based on the comparison of these two formulas against the experiments on a smooth circular cylinder by Sarpkaya (1986). The expression C_{D3} for KC>10 is connected to the effect of vortices "returning" to the body when approaching steady inflow conditions (Faltinsen, 1993). One must note that for KC=0, $C_{D1} \to \infty$. To avoid numerical problems, for KC<0.1, C_D is set equal to the value of C_{D1} at KC=0.1. Moreover, using information from experiments at low and high KC numbers, it is enforced that $0.8 < C_D < 50$ to ensure physical drag coefficients. The six bars have very small cross-section dimensions therefore the drag coefficient for them is set equal to 1.2, assuming steady laminar conditions. The integration of force in (1) leads to 3D force and moment contributions, which are directly expressed in the body fixed coordinate system. In addition to these effects, the bottom of the torus and of the spar experience flow separation when there is a component of the relative velocity along the STC axis. The flow separation is due to the bottom sharp corners. The 3D force induced along the body axis is estimated by splitting the body in vertical strips. In each strip, the problem resembles the facing square cross-section case, but with flow separation only on one side of the body. Therefore, the drag coefficient is assumed independent from KC and equal to 1.5, which is half the value for a square cross-section (Bearman et al., 1984). Integrating the contribution for each vertical strip, we get formally the 3D force as

$$\boldsymbol{F}_{drag,v} = \frac{1}{2}\rho A_{kc} C_D \boldsymbol{v}_{rel} \left|\boldsymbol{v}_{rel}\right| \tag{2}$$

Here, A_{kc} is the wetted area of the bottom, coinciding with the area of the spar cross-section, for the spar, and with the area of the torus cross-section minus the area of the spar cross-section, for the torus. Moreover, $\boldsymbol{v}_{rel}$ is the projection vector along the STC axis of the relative velocity between the incident wave and the platform at the center of the cross-section. It also included a linear viscous damping force acting along the STC axis and given by the friction in oscillatory inflow, i.e.

$$\boldsymbol{F}_{fric,v} = -\nu\rho\sqrt{\frac{\omega}{2\nu}}\pi D_{sp} h_{sp} \dot{\eta}_3 \boldsymbol{k} \tag{3}$$

Here, ω is the incident-wave frequency, D_{sp} and h_{sp} are, respectively, the diameter and draft of the spar, $\dot{\eta}_3$ is the velocity in heave and $\boldsymbol{k}$ is the unit vector along the STC axis.

The local impact solution (B) for the bottom slamming events differs from the modelling in the basic DD. There, the bottom impact of a ship is modelled locally as an impact of a wedge in the cross-sectional plane. In the case of the STC, the impact on the bottom of the torus is expected to start from the outer circle, as far as the incident waves are sufficiently long. Moreover, in this case the impact angle is not between the instantaneous body geometry and a horizontal free

surface, as in the case of a ship with head-sea waves. It is instead, as a rough approximation, the angle in the plane of the incident waves between the instantaneous body surface and the local slope of the incident waves. A strip-theory approach is then applied in the x direction. The local Wagner-type solution for the bottom slamming of a Very Large Floating Structure (Faltinsen et al., 2004) is applied in each strip. At the bottom locations with slamming, the pressure is estimated as the pressure from the slamming solver, which involves the slamming pressure and the added-mass pressure due to time variation of the impact velocity, plus a 'hydrostatic' pressure estimated as relative to the local instantaneous incident-wave elevation. The slamming pressure is the composite solution obtained as matching between the outer and inner solutions of the local impact Wagner-type problem.

The green-water loads are estimated by solver (C) assuming shallow-water conditions for the liquid shipped on the torus deck. This is suitable for water-on-deck scenarios with dam-breaking flow features. The problem is solved on a 2D Cartesian grid on the deck with a splitting algorithm leading to one-dimensional problems along the grid main directions that are solved in cascade in time. A first-order time marching scheme is adopted since it has proved to be efficient and accurate for relatively long time simulations. The fluxes involved in the shallow-water equations are estimated with a local Riemann solver. The boundary conditions on the deck profile and on the deck superstructure (in the present case, respectively, the outer circle of the torus and the circle of the spar) are enforced using a Level-Set function (see e.g., Colicchio et al., 2005) to identify the boundary. At the deck profile, both inflow (water on deck) and outflow (water off deck) conditions are modelled. During the water-on-deck phase, the level of the water entering the deck and its velocity are provided along the deck profile. The water level comes from the local relative vertical motion between the body and the incident, radiation and scattering waves; the water velocity is estimated as projection on the deck of the local relative velocity between the body and the incident waves. The green-water induced loads are estimated on the deck while no model is considered for impact loads on the superstructure.

All loads are expressed in the body-fixed reference frame. Then the STC accelerations can be estimated and integrated in time. This gives the body velocities, which are projected in the Earth-fixed reference frame and integrated in time to get the translations of the platform and the Euler angles (see e.g. Faltinsen, 2005). As in the basic DD, the motion equations are solved in time by using a Runge-Kutta fourth-order scheme. The scattering, Froude-Krylov and hydrostatic loads are estimated at all intermediate time instants within a Runge-Kutta time step Δt, while the other loads are estimated at the beginning of the time step and then kept constant during Δt. Within the solution algorithm, at time t, solver (C) takes the information from solver (A) in terms of body motions, velocity and accelerations and uses them to estimate the boundary conditions along the deck profile and to integrate in time the shallow-water equations written in the accelerated reference frame between t and $t+\Delta t$. Similarly, solver (B) takes the information from solver (A) in terms of body motion, velocity and acceleration, to estimate relative motion, impact velocity and time variation of the impact velocity needed for the slamming solution algorithm and in the expression of the pressure. At the end of these time integrations, the green-water loads $\boldsymbol{F}_{wod}$ and the slamming loads $\boldsymbol{F}_{slam}$ are estimated and provided to solver (A). In general, the time steps of the WOD and of the SLAM solvers are smaller than Δt.

In the following, the described numerical method is referred to as nonlinear solver because of the nonlinear modelling of the slamming and water-on-deck loads. However, one must note that it is not a fully nonlinear method because it assumes linear radiation and scattering effects and includes nonlinear contributions in the Froude Krylov and hydrostatic loads. We expect that the numerical predictions are less reliable for incident wavelength comparable or smaller than the characteristic body length and that a limit exists in terms of incident-wave steepness. The next section examines quantitatively the solver predictions through validation studies on the STC concept in regular waves, also for cases with strongly nonlinear wave-body interaction features. Then, the method is used to complement the model tests within a physical investigation.

4. Validation of the nonlinear solver and combined experimental-numerical physical investigation

The validation analysis of the nonlinear solver against the experiments is performed comprehensively for all the incident wave cases with largest wave height tested, i.e. H=9 m, leading to WEE phenomena. Some comparisons for the cases with

H = 2m are also reported to help the physical investigation. The wave period T=2π/ω, both in full and model scale, wave steepness kA and non-dimensional wave length λ used in the regular wave tests chosen for the validation are presented in Table 5. Here, A= ζ_a is the wave amplitude. The wave period in full scale T_{full} changes between 9s and 15s, and the wave height H is kept equal to 9m (in full scale) for all cases. As a consequence, the prescribed wave steepness ranges between 0.08 and 0.22. One must note that the incident-wave measurements indicated some differences in the height of the generated waves. The actual wave steepness is also provided in the table; however, for convenience the nominal incident-wave parameters are indicated in the text. For the examined cases, the wave length λ to torus outer diameter D_{torus} ratio is larger than 6.32.

The numerical results discussed in the following have been obtained using a time step Δt=T/200 to ensure convergent results when performing the time integration. T refers to the wave period. The submerged part of the spar-torus system in the mean configuration was discretized with 3054 panels almost uniformly distributed with maximum size about $0.068D_{torus}$. Because the incident waves are longer than $6.32D_{torus}$ and the radiated and diffracted waves are linear, this ensures converged results for the linear quantities. The dry part (up to the torus freeboard) was discretized with 4760 panels almost uniformly distributed with maximum size about $0.033D_{torus}$. This was done to properly capture the freeboard exceedance during water shipping events. The torus deck within the shallow-water solver for the water shipping was discretized with a Cartesian grid size about $0.01D_{torus}$. The numerical convergence was checked by comparing against the results with deck grid size $0.005D_{torus}$ for the case with T_{full} = 13s and H = 9m.

Table 5. Wave period (full and model scale), prescribed and actual measured wave steepness and non-dimensional wave length in the regular wave tests chosen for the validation of the nonlinear solver under wave height of 9 m in full scale.

T_{full}	9	11	12	13	14	15
T_{mod}	1.27	1.56	1.70	1.84	1.98	2.12
kA	0.22	0.15	0.13	0.11	0.09	0.08
kA_{actual}	0.20	0.17	0.14	0.11	0.09	0.08
λ/L	6.32	9.44	11.24	13.19	15.30	17.56

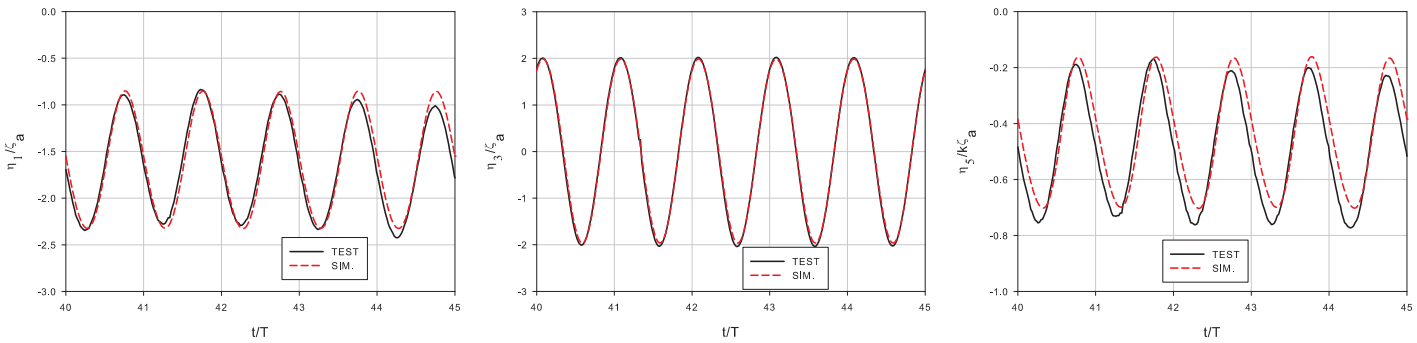

Figure 7. Surge (left), heave (middle) and pitch (right) motions in the regular wave case with H=9m and T=15s from the experiments and the numerical solution.

The motions in almost steady-state conditions from the model tests and the nonlinear simulations are investigated first. Figure 7 shows the time evolution of surge, heave and pitch motions for the incident-wave case at T=15s. Experiments and numerical results show an overall satisfactory agreement both in terms of amplitudes, phases and mean value. Limited discrepancies are observed only for the pitch motion. They seem to be connected with a small modulation of the experimental envelop curve.

Figure 8 to Figure 10 show the comparison between experiments and numerical results for the cases reported in Table 5, through the non-dimensional amplitude of first- (ω; Figure 8), second-order (2ω; Figure 9) harmonics and the mean values (Figure 10) of the surge (left panel), heave (center panel) and pitch (right panel) motions. For the second order harmonics

and the mean values of the motions, surge and heave motions are divided by kA^2, and pitch motions are divided by $(kA)^2$ to obtain the non-dimensional values. The wave amplitude and steepness used for the non-dimensional variables from the experiments and the numeric are consistent with the physical and simulated incident waves, respectively. To investigate the WOD and SLAM effects on the motions, the nonlinear simulations without considering WOD and SLAM are also carried out and the results are included in Figure 8 to Figure 10. One must note however that from our study (Wan et al., 2016b), the slamming effect on the platform motions is very limited. The study in this paper also shows insignificant slamming effects on body dynamic motions. Therefore, possible differences between the results without and with these nonlinear phenomena are associated mostly to the water shipping loads.

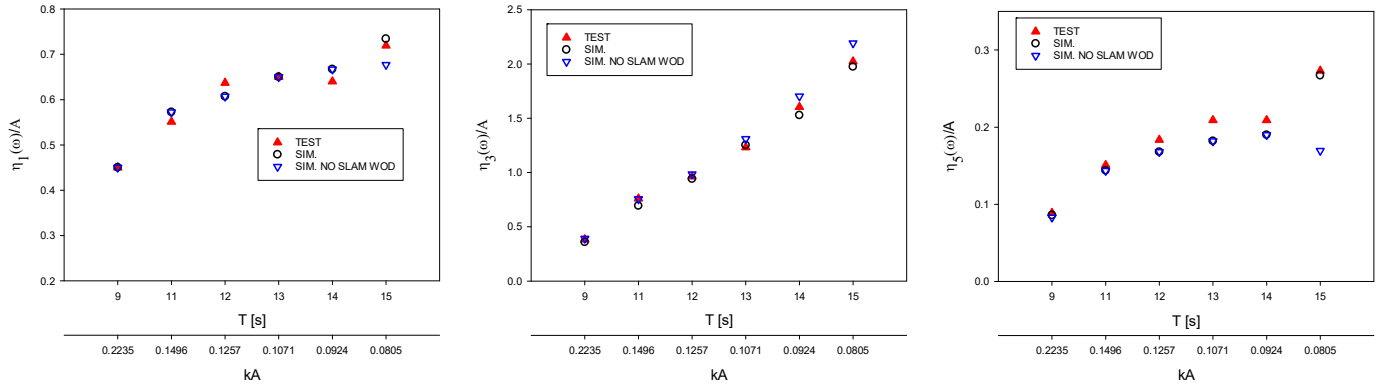

Figure 8. Non-dimensional amplitude for the first-order harmonics of the surge (left) heave (middle) and pitch (right) motions from the experiments and the nonlinear solution versus the incident-wave period and the prescribed incident-wave steepness.

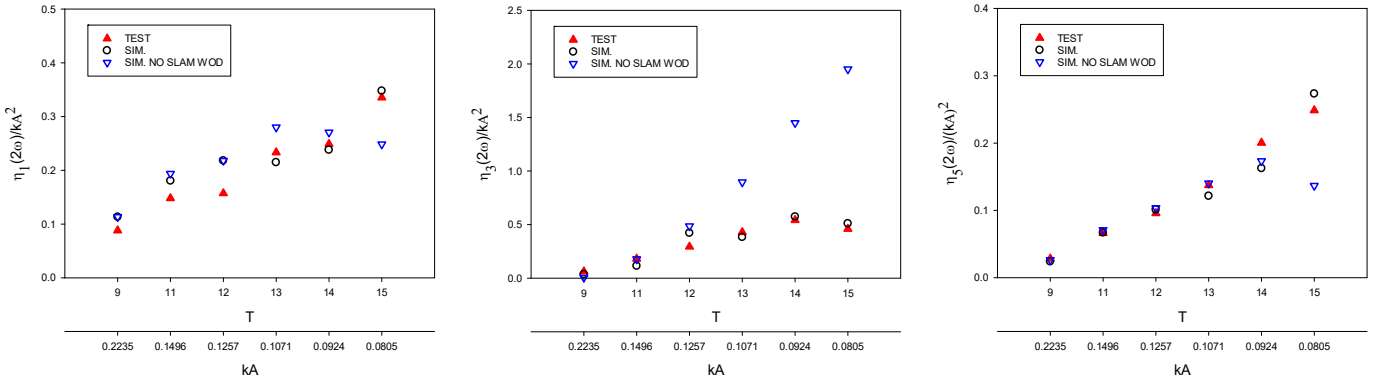

Figure 9. Non-dimensional amplitude for the second-order harmonics of the surge (left) heave (middle) and pitch (right) motions from the experiments and the nonlinear solution versus the incident-wave period and prescribed incident-wave steepness.

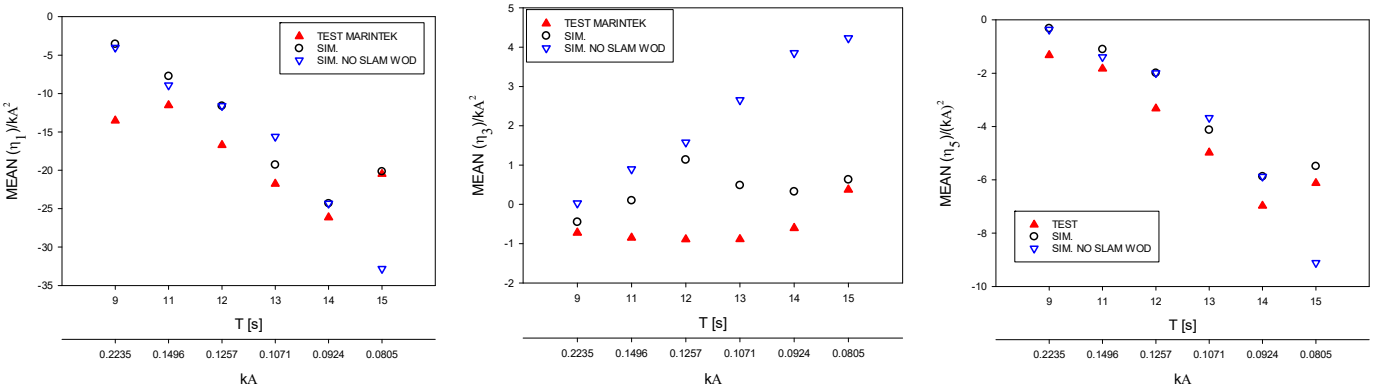

Figure 10. Non-dimensional mean values for surge (left) heave (middle) and pitch (right) motions from the experiments and the nonlinear solution versus the incident-wave period and prescribed incident-wave steepness.

The amplitude of the first-order harmonic of the motions increases with the incident-wave period, within the examined range, and is well predicted by the numerical method. The largest differences are observed for the pitch that is slightly underestimated for T between 12 and 14 s. The influence of WOD loads is limited for the horizontal motion. For heave and pitch, it becomes more pronounced at the largest incident wave periods and tends to lower and push bow-down the platform.

The magnitude of the second-order harmonic components is small when compared to the first-order contribution for all examined motions. The ratios of the second-order harmonic to the first-order harmonic for all the motions are lower than 5% according to the estimation. This implies a larger sensitivity to the experimental errors. Despite this, good agreement is achieved for the second-order harmonic responses between the nonlinear solver and the model tests. The largest disagreement with the measurements are observed for the non-dimensional mean surge motion at T=9 s, for which the numerical WOD loads appear limited.

The numerical model, confirming the experimental observation about the occurrence of the WOD, is used here to discuss the source and the relevance of the second-order contributions. Figure 9 shows that WOD has a strong effect on the second-order harmonic, in particular for the vertical motions and at larger period of the incident wave. This is mainly connected with the massive amount of water entering the deck. A similar trend is observed for the surge motion, although larger discrepancies are evident, in particular in the range close to the heave natural period. The effect of the WOD is also confirmed in the mean value component shown in Figure 10, although there are some differences for the heave motion with respect to the experiments. The discrepancies could be connected with a limitation of the nonlinear solver, which uses a direct-pressure integration for the loads. The latter can lead to numerical challenges in terms of accuracy and convergence of the results. The experimental identification of the mean motions is also a difficult task, because of the possible influence of spurious low frequency term related to the seiching mode of the basin. The WOD effect is quite important at sufficiently large T and tends to reduce the mean values of all the motions.

To assess the effects of the total WEE of the torus on motions from the model tests, the non-dimensional surge, heave and pitch have been compared against the corresponding values for incident waves with H=2 m. For the cases with H=2 m, WEE of the torus, SLAM and WOD did not occur, but for T=13s where limited slamming and water on deck phenomena were observed. Figure 11, Figure 12 and Figure 13 show the non-dimensional mean, first-order harmonic and second-order harmonic motions, respectively. The results confirm a good agreement in terms of trends between measurements and numerical results at H=2 m. They are also quantitatively close but for the surge and pitch at T=12 and 13 s. In this case, the experiments indicate much larger absolute mean and first-order surge and pitch values than the numerical results for the region of heave resonance. The discrepancies in surge and pitch at resonant region are partially explained with greater sensitivity, near the resonance, of the response variables to differences in the damping level. The absolute mean heave is approximately 1% of the absolute first order harmonic of the heave motion at H=2 m, while it is approximately 10% at H=9 m cases. This indicates the significant mean heave caused by the total WEE of the torus accompanied by WOD and slamming. The comparison of the motion quantities at H=2 m and H=9 m indicates that the total WEE of the torus accompanied by the WOD and slamming effect reduces all the motions in the heave-resonance region. The influence tends to become negligible at lower T. At larger incident-wave periods, the influence is limited.

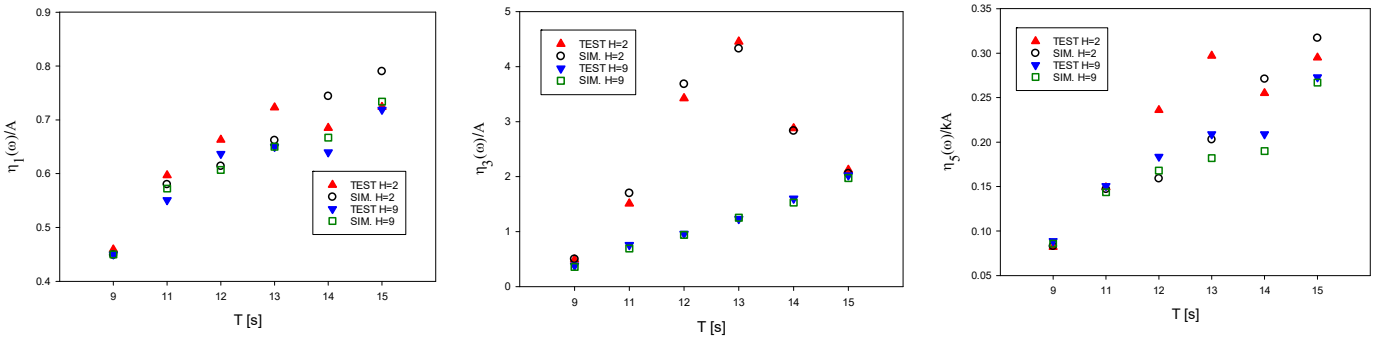

Figure 11. Non-dimensional amplitude for the first-order harmonics of the surge (left), heave (middle) and pitch (right) motions from the experiments and the nonlinear solution versus the incident-wave period for the two wave heights H= 2 m and 9 m.

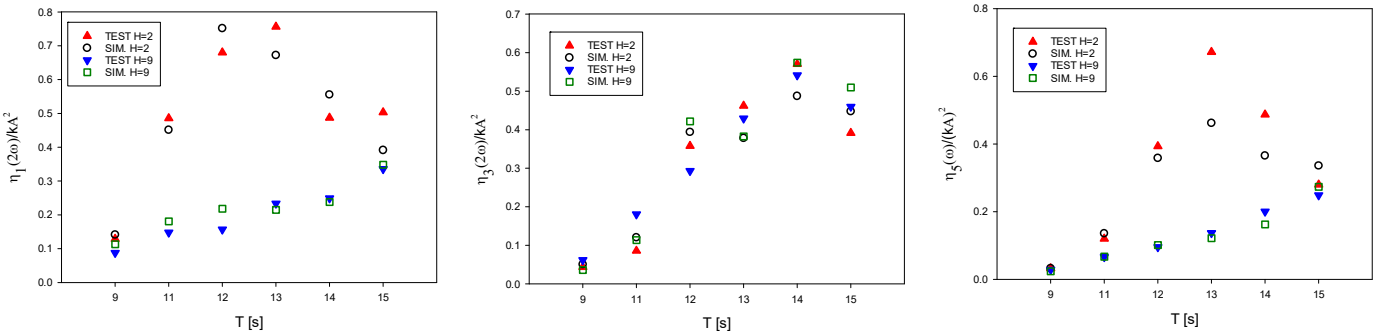

Figure 12. Non-dimensional amplitude for the second-order harmonics of the surge (left), heave (middle) and pitch (right) motions from the experiments and the nonlinear solution versus the incident-wave period for the two wave heights H= 2 m and 9 m.

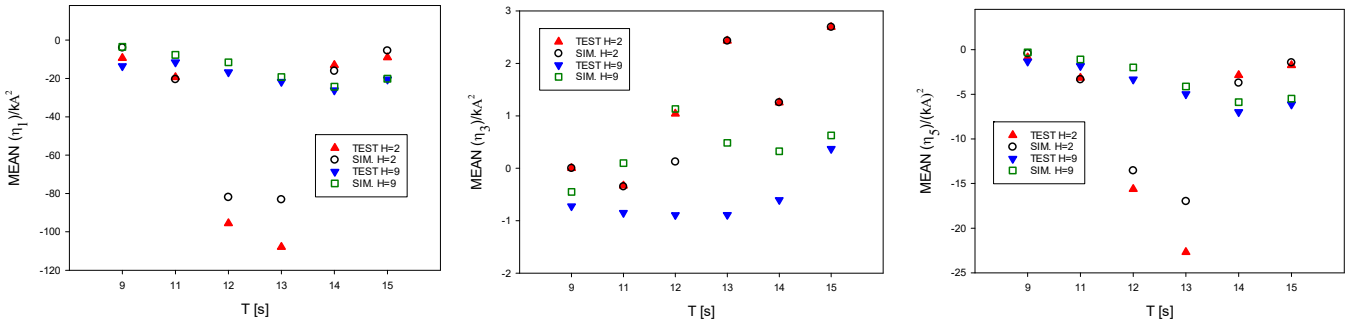

Figure 13. Non-dimensional mean values for surge (left), heave (middle) and pitch (right) motions from the experiments and the nonlinear solution versus the incident-wave period for the two wave heights H= 2 m and 9 m.

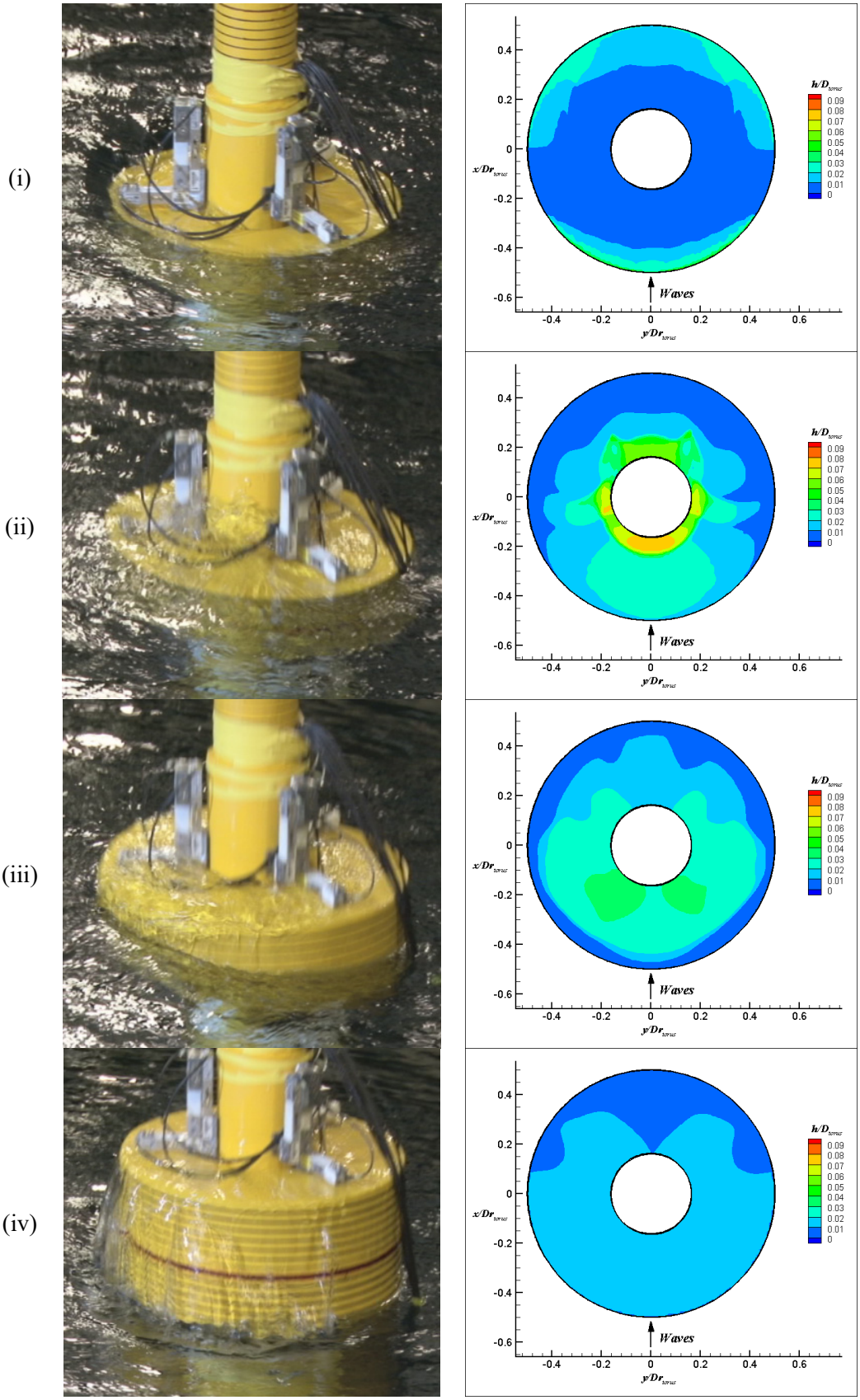

Figure 14. Water on deck for case with T=15s and H=9m. Left: experimental snapshots (the incident wave travels from left to right). Right: numerical water level h along the torus deck made non dimensional by the torus diameter D_{torus} (the incident wave travels from bottom to top). Time increases from top to bottom.

The typical evolution of the shipped water on the torus deck in long waves is shown in Figure 14 as recorded in the experiments and predicted numerically. The examined incident-wave case refers to T=15s and H=9m. Time instants

increase from (i) to (iv) and show consistency between the two solutions. Time instant (i) corresponds to the start of the WOD, when green water invades the torus deck from the outer circle in the incident and leeside wave directions; time instant (ii) shows a moment with a large amount of green water on deck and with water hitting the tower from incident wave direction; time instant (iii) represents the stage that green water leaves the torus deck as the torus is going upward; the last stage shown as time instant (iv) corresponds to the moment when there is nearly no green water left on the torus deck.

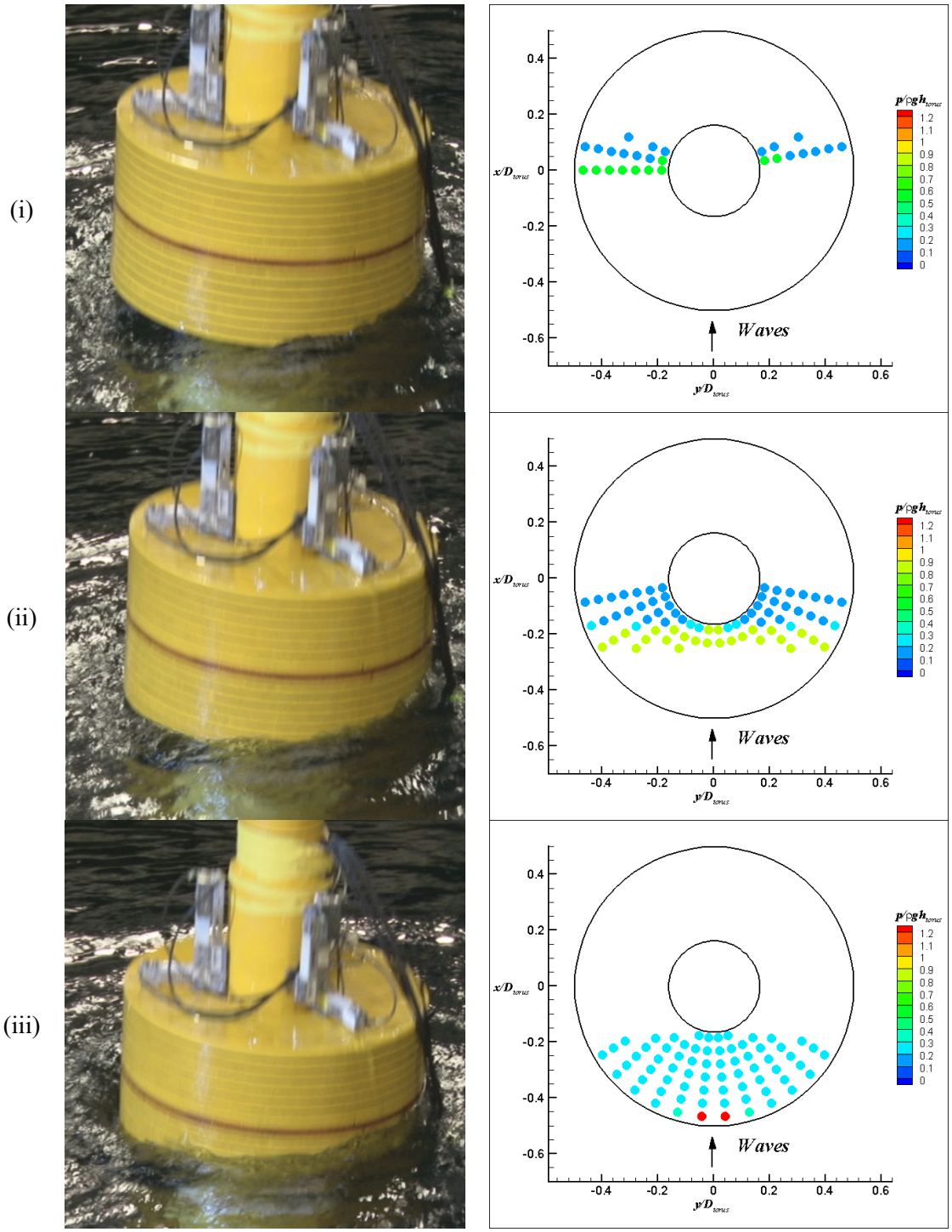

Figure 15. Water entry for case with T=15s and H=9m. Left: experimental snapshots (the incident wave travels from left to right). Right: numerical slamming pressure p along the torus bottom made non dimensional by $\rho g h_{torus}$, with h_{torus} the torus draft (the incident wave travels from bottom to top). Time increases from top to bottom.

From the experimental snapshots, the corresponding water-entry phase starts from the aft part of the torus bottom, as shown in Figure 15. This occurs also in the simulation. From the numerical slamming-pressure results (time increases

from (i) to (iii)), near the aft part of the bottom the wave-induced pressure is limited and does not satisfy the slamming criteria (Greco and Lugni, 2012). The pressure raises to slamming levels towards the center of the torus bottom as shown in (i); then the impact area moves from leeside to the wave side, covering a larger area of the torus bottom (ii) and reaches the highest values near the front part of the bottom (iii).

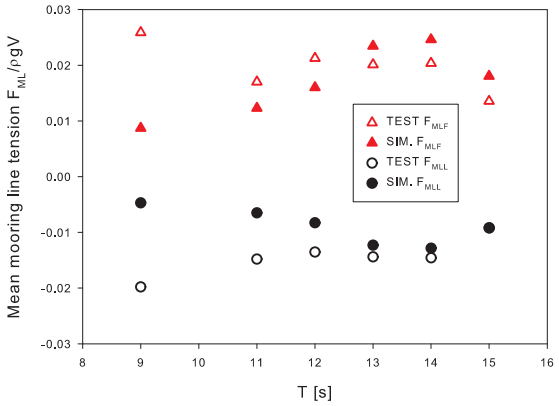

Figure 16. Non-dimensional mean mooring-line tensions F_{MLF} and F_{MLL} from the experiments and the nonlinear solution versus the incident-wave period (pretensions are subtracted).

The discrepancy at T=9s in surge motion between experimental and numerical results in Figure 10 is confirmed by the mean non-dimensional mooring line tensions F_{MLF} and F_{MLL} provided in Figure 16. The numerical model and the model tests are consistent for all incident waves except for the case with T=9s, associated experimentally with much larger mean tension for the mooring-line in the wave side and much less mean tension for the mooring lines in the leeside than predicted numerically.

(i)

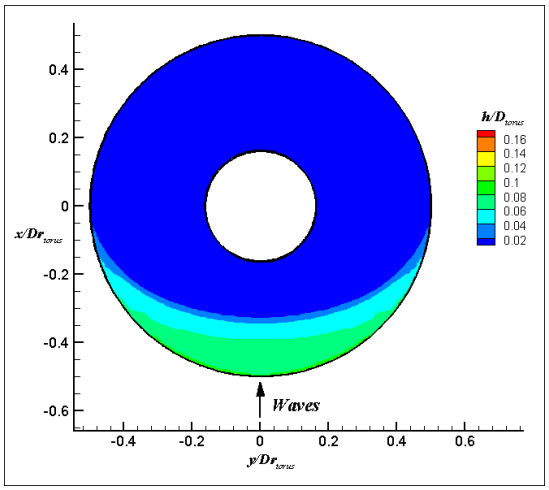

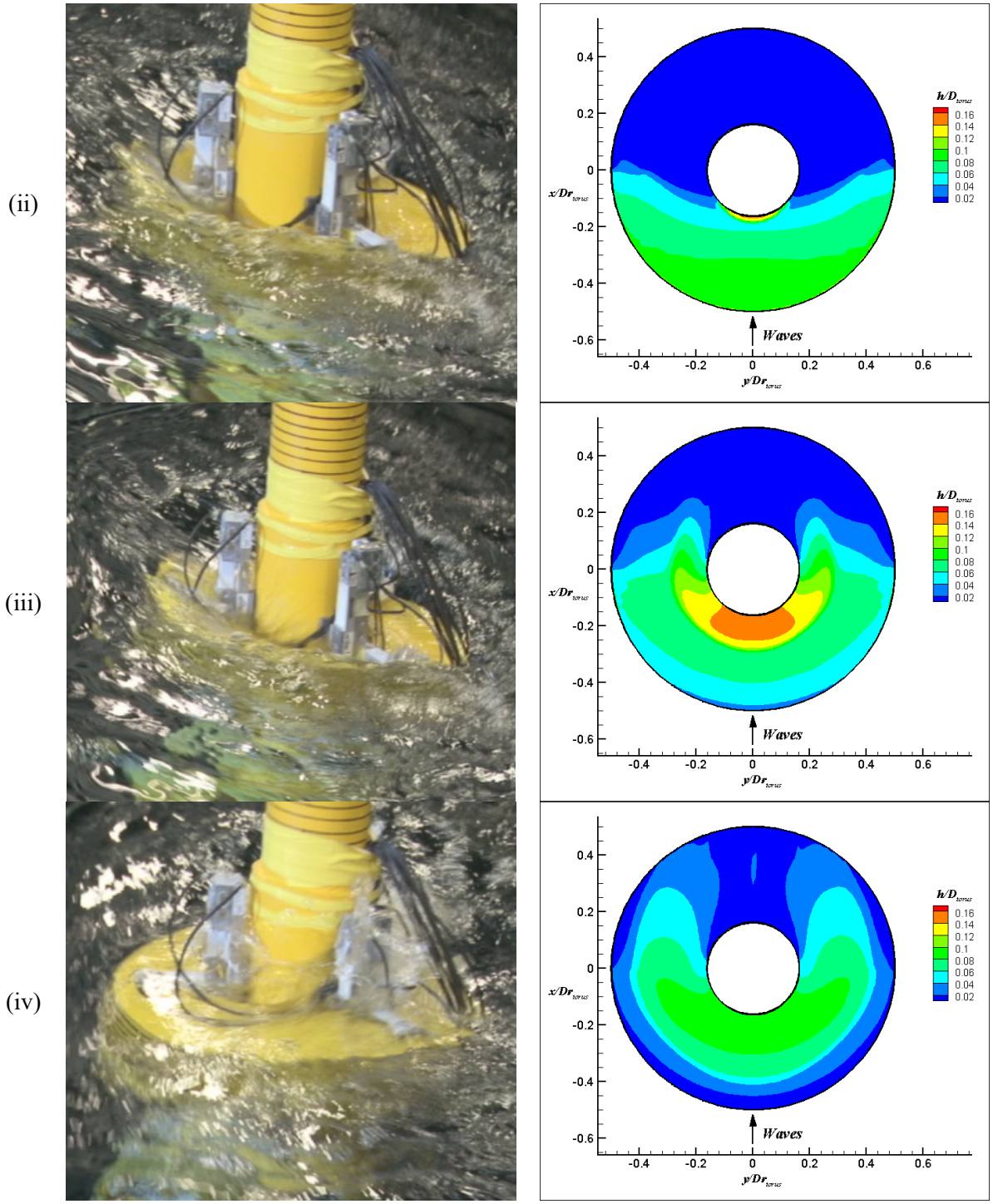

Figure 17. Water on deck for case with T=9s and H=9m. Left: experimental snapshots (the incident wave travels from left to right). Right: numerical water level *h* along the torus deck made non dimensional by the torus diameter D_{torus} (the incident wave travels from bottom to top). Time increases from top to bottom.

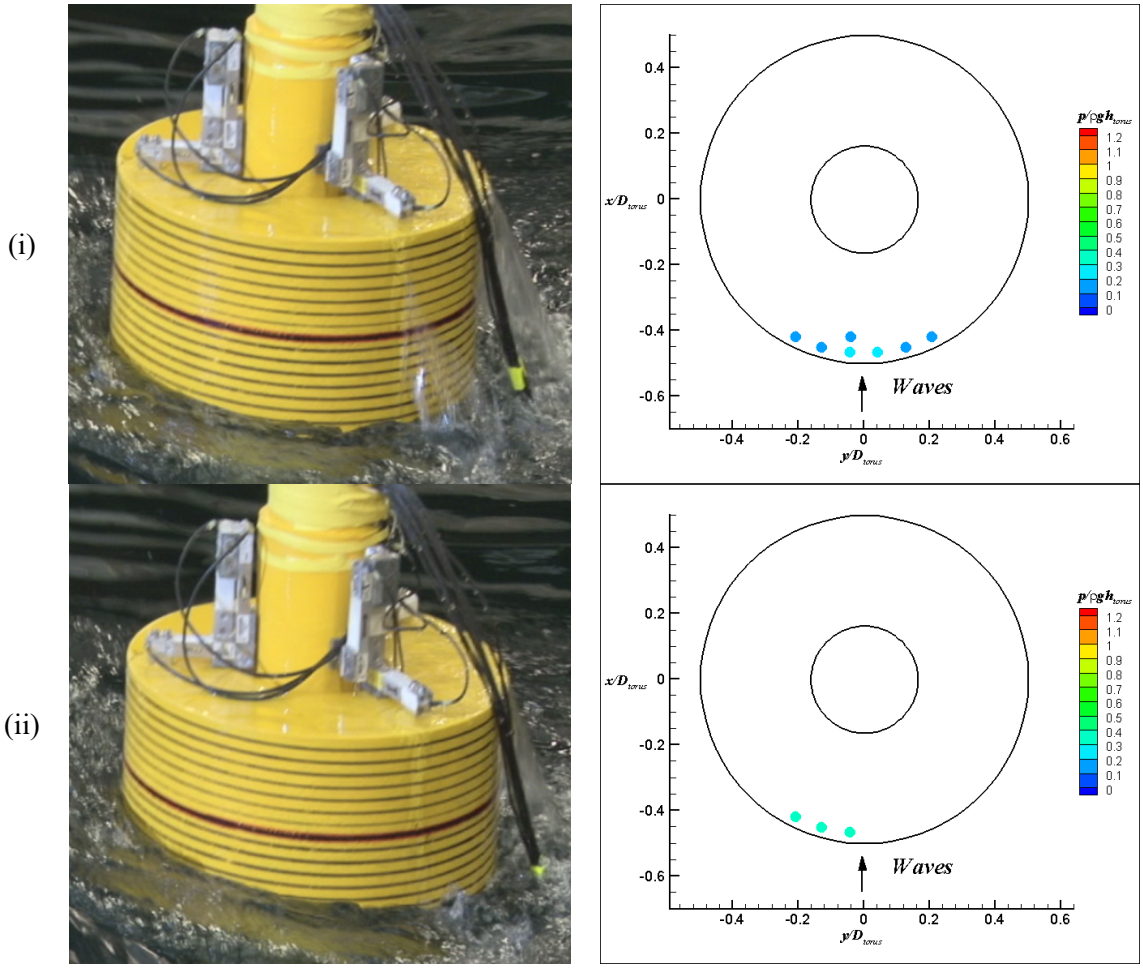

Figure 18. Water entry for case with T=9s and H=9m. Top: experimental snapshots (the incident wave travels from left to right). Bottom: numerical slamming pressure p along the torus bottom made non dimensional by $\rho g h_{torus}$, with h_{torus} the torus draft (the incident wave travels from bottom to top). Time increases from top to bottom.

The incident wave with H=9 m and T=9 s corresponds to the steepest case examined experimentally and causes WEE and WOD events with different features with respect to the other examined waves, as shown in Figure 17 and Figure 18. In this case, water-on-deck and bottom-impact events start from the front bow of the torus. The numerical method is able to capture qualitatively this, therefore the reasons of the discrepancies must be found elsewhere. Contributing factors could be: 1) the measurements of the incident-wave elevation indicate important nonlinear features with pronounced flattened troughs and some left-right asymmetry, while the numerical incident waves are based on the second order wave theory; 2) the wave-body interactions in the model test lead to nearly breaking waves near the platform. They hit against the front bow of the torus. The numerical method does not model impacts on the front bow; 3) the shipped water hits the spar above the torus deck. Also this impact phenomenon is not modelled in the numerical method; 4) the mooring line in the front of the torus experienced dynamic problems in the model test (Wan et al., 2015): springs were used in the model test to achieve the restoring effect of the mooring lines in the full-scale design. However, a combination of four springs was used for the mooring line in the front of the torus and this leads to a large weight of the springs and induces the dynamic effect in the spring tension (i.e. the inertia forces from the springs), which are not modeled in the numerical simulation. In addition, the fore-aft asymmetry in the WOD and WEE phenomena suggests a greater sensitivity of the wave-body interaction to the set-up of the mooring-line system used in the experiments with respect to other incident-wave cases. This would suggest the mooring-line modelling as an important contribution to the documented disagreement.

The numerically predicted occurrences of slamming and green water for all examined cases are shown in Figure 19. They are identified, respectively, by the value -1 of the horizontal solid red lines and by the value 1 of the horizontal dashed green lines. The horizontal thick orange lines represent the top (positive value) and bottom (negative value) of the torus as described in Figure 5. The incident wave elevation and the approximated relative vertical motion from model tests, as

described in section 2.2, are also presented. The results indicate slightly longer duration of water shipping relative to the incident-wave period, as T reduces. The slamming events seem to last for a similar percentage of T in all examined incident waves. The numerically predicted WOD and SLAM occurrences agree fairly well with their occurrences estimated from the approximated relative vertical motion s_r, but for the case with H=9m and T=9s. The small differences for the longer waves and the larger discrepancies for the shortest wave can be partially justified by the fact that s_r does not account for the pitch motion and considers only the measured incident wave, while in the nonlinear numerical solver, the linear diffracted and radiated waves are accounted for when estimating the vertical relative motion between the local platform point and the liquid.

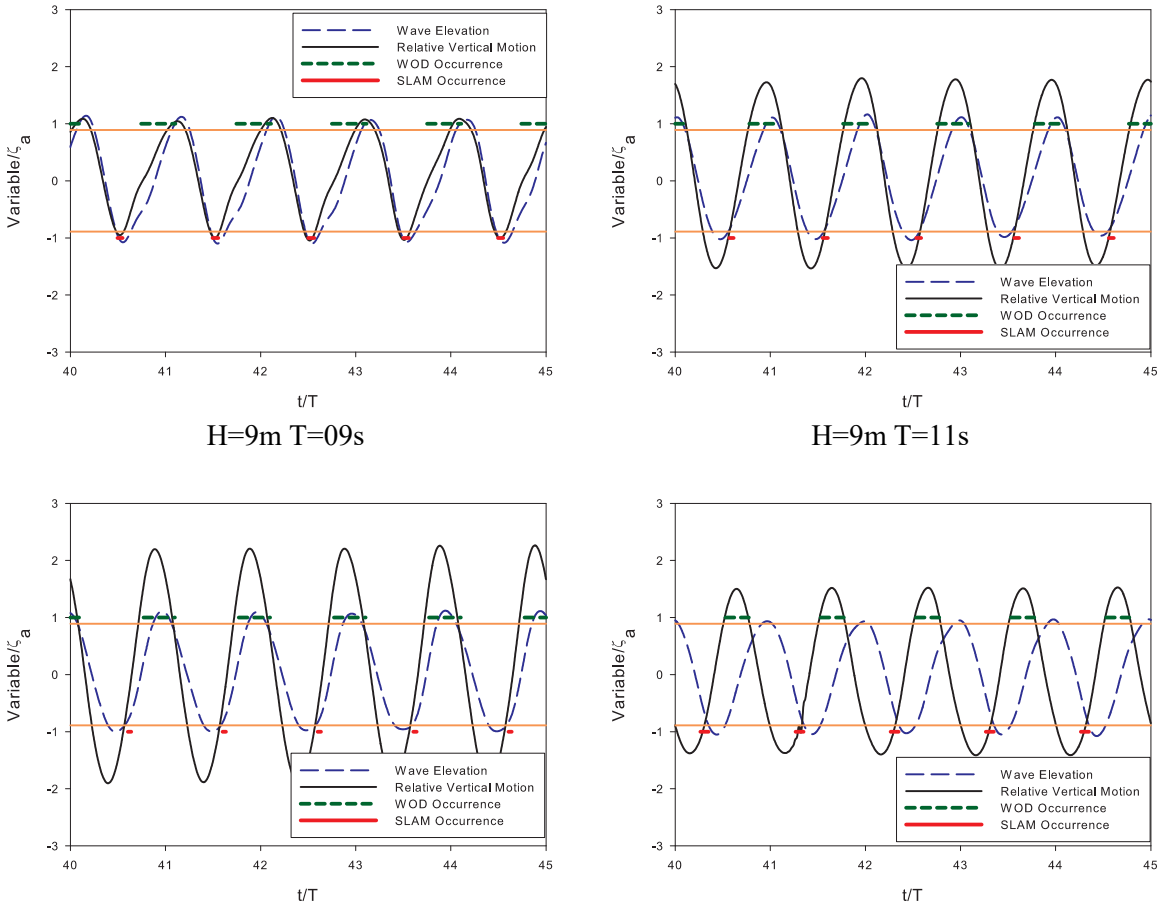

H=9m T=09s H=9m T=11s

H=9m T=13s H=9m T=15s

Figure 19. Numerical predictions of the occurrence of slamming and green water for cases with H=9m and T=9s (top left), T=11s (top right), T=13s (bottom left) and T=15s (bottom right), respectively. The thick horizontal orange lines represent the top (positive value) and the bottom (negative value) of the torus.

In the model tests, the pressures on the torus bottom were not measured. On the other hand, because the slamming local loads usually show a strong random character (see e.g. Faltinsen (2005), Lugni et al. (2006, 2010)), the local pressure is not a reliable physical quantity to examine. We measured instead the interface forces, i.e. the relative forces exchanged between the spar and the torus system. Although this is a global measure of the load, it is strongly affected by the impulsive load induced by the slamming as discussed in sections 2.2 and 2.3. To measure such forces, load cells were mounted between the spar and the torus. They acted as a spring-damper system connecting the spar and torus masses. It means that very small relative heave motion (typical of the strain gauge load cells) is allowed between the two bodies. The interface forces were estimated as sum of the force contributions measured by all load cells.

In the proposed numerical solver, the STC concept is modelled as a single body, which means the interface forces between the torus and the spar cannot be directly estimated. Therefore, the SIMO platform is used to model the spar and the torus as a two-body system with spring-damper features consistent with the experimental load cells and with slamming

loads provided by the nonlinear numerical solver. For each examined incident-wave case, because the slamming force peaks predicted in different slamming events demonstrate stochastic distributions, their mean value is used in the simulation in SIMO, while the exact wave impact duration is considered. The time series of the vertical interface force Fz from the model tests and the simulations with and without considering slamming are shown in Figure 20 for two incident-wave cases with H=9m, T=11s and with H=9m, T=13s.

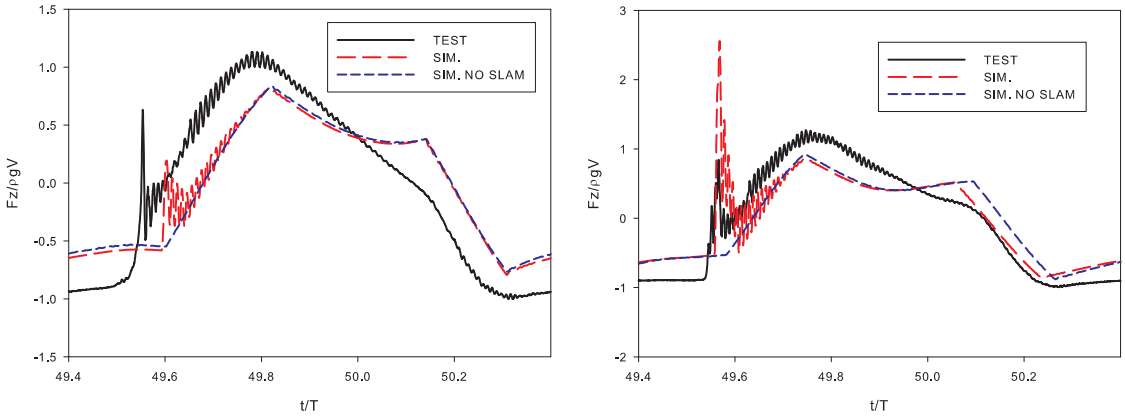

Figure 20. Non-dimensional vertical interface force responses Fz/ρgV from the model tests and the numerical simulation for incident waves with H=9m, T=11s (left) and with H=9m, T=13s (right).

After the impact phenomena, the vertical interface force in the tests shows a rising phase followed by a peaked behavior and by high-frequency oscillations with period T_{nT} = 0.0163s (in model scale). T_{nT} corresponds to the natural period of the mass-spring-damper system described above. Because the rising time of the slamming force is comparable to T_{nT}, one cannot exclude hydroelastic excitation in the model tests. The numerical interface forces from SIMO are also characterized by oscillations induced by the slamming, with period T_{nS} = 0.0159s (in model scale). The time evolution is similar to the measurements, though with a difference in the maximum amplitude. This might suggest a role of the hydroelasticity, not accounted for in the numerical solution. The hydroelasticity here refers to the eigenmode of the relative heave motions of the spar and the torus connected by the load cells (as a spring-damper system), not the vibrational modes of the local structure on the bottom of the torus. Another reason for the difference could be the use of mean slamming loads for the interface-force predictions, as explained above. The oscillations damp out in time due to the involved damping, which seems to be lower in the model tests.

In the experiments, it is difficult to determine the exact starting time of the slamming impact, while in SIMO, we can determine the starting time of the slamming impact by the relative vertical motion s_r. It is not possible to have a consistent comparison between SIMO and model test on the first peak if we are not clear about the starting of the slamming in the model test. In this case, the difference between the first peak and the first trough of the oscillations is used in the comparison between numerical and experimental results.

In this work, F_{SLAM_PEAK} represents the mean values of the slamming peaks from the nonlinear solver. This is also the input for the SIMO simulation and the excitation load for the interface force. F_{NUM_1} is the first interface-force peak from the start of the slamming in SIMO; F_{NUM_2} represents the interface-force difference between the first peak and first trough of the oscillations in SIMO. F_{NUM_1} and F_{NUM_2} are constant for all the slamming events in the same regular wave case. From the model tests, F_{TEST_2} is the value of the interface-force difference between the first peak and the corresponding first trough of the slamming event in the test. F_{TEST_2MEAN}, F_{TEST_2MAX}, and F_{TEST_2MIN} are the mean, maximum and minimum values of F_{TEST_2}, respectively, in all the slamming events in one regular wave case. The symbols are demonstrated in the left plot of Figure , and the values of the symbols are shown in the right plot. The maximum numerical slamming response, i.e. the maximum interface force F_{NUM_1} is similar to F_{SLAM_PEAK}, which means the transfer function is close to 1. The numerical interface-force difference between the first peak and the first trough, i.e. F_{NUM_2}, is smaller than F_{TEST_2MAX} and larger than F_{TEST_2MIN}. This means F_{NUM_2} is in the range of the slamming responses in the

model tests. Considering that the slamming responses in the model test show stochastic property, the slamming pressure prediction is in a reasonable range. As Fz, the interface force in x direction, Fx (not shown here) is also strongly affected by the water exit and entry process and the slamming and water on deck phenomena.

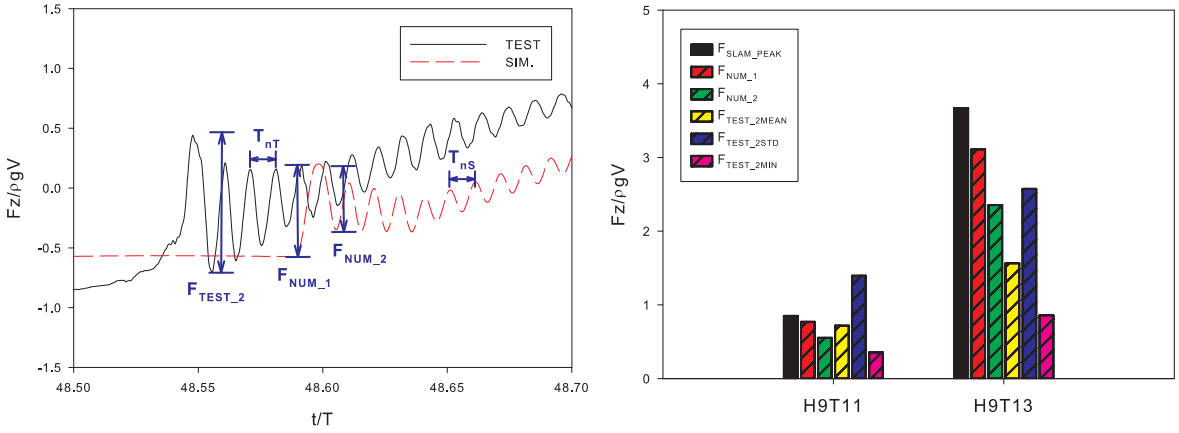

Figure 21. Interface force response in z direction. Left: time series under slamming in the case with H=9m and T=11s and the relevant variables defined. Right: values of the force variables defined in the main text for H=9m and T=11s and with H=9m and T=13s.

Conclusions and future work

In this work, a blended method based on potential-flow theory with viscous corrections for the damping loads is used to simulate the strongly nonlinear phenomena, i.e., water entry and exit, as well as the slamming and green water observed in the mean water level (MWL) survivability model test of a combined wind and wave energy converter device, named STC concept.

The features of experimental water entry and exit phenomena are investigated. The assessment of occurrence of slamming and water on deck by an approximated relative vertical motion, based on the incident-wave elevation and on the heave motion only, is found to be reasonable if the incident wave is long enough compared with the torus diameter, although local error exists. The spar-torus interface forces Fx and Fz are strongly affected by the water exit and entry process and the slamming and water on deck phenomena.

The nonlinear numerical solver provides good predictions with respect to both motions and mooring-line tensions compared with the model test but for the steepest incident-wave case examined, corresponding also to the shortest incident wave, which is associated with strongly nonlinear phenomena and impact events not modeled in the adopted solver. Occurrences and features of WEE and WOD phenomena agree with the model tests. The combined experimental-numerical analysis showed different scenarios of WEE and WOD events for the shortest and steepest waves and the other examined incident-wave conditions. For longer and less steep waves, the slamming starts from the center of the torus bottom; the water shipping occurs almost contemporary from the wave and lee side of the deck. In the shortest examined wave, both water shipping and slamming phenomena start from the wave side. The fore-aft asymmetry in the WEE and WOD phenomena suggests a greater sensitivity of the wave-body interaction to the mooring-line set-up used in the experiments with respect to other incident-wave cases. This could partially explain the documented disagreement in the mean mooring-line tensions and other variables for this case. Other possible reasons have also been examined in section 4, including the dynamic effect of the mooring springs in the model test.

From the analysis it was found that the WOD is very effective in reducing the 2ω component of the surge, heave and pitch motions for sufficiently large incident-wave periods, and in reducing the mean surge and pitch motions close to the heave resonance. In cases with H=2 m, there is no total WEE with WOD and slamming of the torus. The total WEE of the torus reduces all the motions in the heave-resonance region. The influence tends to become negligible at lower T. At larger

incident-wave periods, the influence is limited. The slamming effects on the platform motions appear negligible while an important influence is found in the interface forces acting between the spar and the torus, both in terms of local peaked behavior and of oscillations excitation for the mass-spring-damper system resulting from the experimental set-up. The interface forces predicted numerically with a two-body (spar-torus) modelling from SIMO including the spring-damper features as in the experimental set-up and slamming loads from the nonlinear solver agree fairly well against the experiments.

The next step of the research will consider a systematic investigation of the incident-wave parameters using the nonlinear method and its further validation for the occurrence and features of parametric pitch resonance.

Acknowledgements

The authors gratefully acknowledge the financial support from the European Commission through the 7th Framework Programme (The MARINA Platform Project –Marine Renewable Integrated Application Platform, Grant Agreement 241402), the support from Research Council of Norway through the Center for Ships and Ocean Structures (CeSOS) and the Centre for Autonomous Marine Operations and Systems (project number 223254) at NTNU, as well as the support from the China Scholarship Council (CSC).

References

Bearman, P., Graham, J., Obasaju, E., Drossopoulos, G., 1984. The influence of corner radius on the forces experienced by cylindrical bluff bodies in oscillatory flow. Applied Ocean Research, 6 (2), 83-89.

Colicchio, G., Landrini, M., Chaplin, J.R., 2005. Level-Set Computations of Free Surface Rotational Flows. Journal of Fluids Engineering, 127 (6), 1111-1121.

Cummins, W., 1962. The impulse response function and ship motions. SchiffStechnik, 47 (9), 101-109.

Faltinsen, O.M., 1993. Sea loads on ships and offshore structures. Cambridge university press.

Faltinsen, O.M., 2005. Hydrodynamics of high-speed marine vehicles. Cambridge university press.

Faltinsen, O.M., Landrini, M., Greco, M., 2004. Slamming in marine applications. Journal of Engineering Mathematics, 48 (3), 187-217.

Greco, M., Bouscasse, B., Lugni, C., 2012. 3-D seakeeping analysis with water on deck and slamming. Part 2: Experiments and physical investigation. Journal of fluids and structures, 33, 148-179.

Greco, M., Lugni, C., 2012. 3-D seakeeping analysis with water on deck and slamming. Part 1: numerical solver. Journal of fluids and structures, 33, 127-147.

Greco, M., Lugni, C., Faltinsen, O.M., 2014. Can the water on deck influence the parametric roll of a FPSO? A numerical and experimental investigation. European Journal of Mechanics - B/Fluids, 47 (5), 188–201.

Greco, M., Lugni, C., Faltinsen, O.M., 2015. Influence of motion coupling and nonlinear effects on parametric roll for a floating production storage and offloading platform. Philosophical Transactions, 373 (2033).

Luan, C., Michailides, C., Gao, Z., Moan, T., 2014. Modeling and analysis of a 5 MW semi-submersible wind turbine combined with three flap-type wave energy converters, 33rd International Conference on Ocean, Offshore and Arctic Engineering, San Francisco, USA.

Lugni, C., Brocchini, M., Faltinsen, O. M., 2006, Wave impact loads: the role of the flip-through, Physics of Fluids 18 (12), 122101-1,17.

Lugni C., Brocchini M., Faltinsen O.M., 2010, Evolution of the air-cavity during a depressurized Wave Impact. Part II: the dynamic field. Phys. Fluids 22 (5), 056102-1,13.

Lugni, C., Greco, M., Faltinsen, O.M., 2015. Influence of yaw-roll coupling on the behavior of a FPSO: An experimental and numerical investigation. Applied Ocean Research, 51, 25-37.

MARINTEK, 2007. SIMO User's Mannual Version 3.6.

MARINTEK, 2014. http://www.sintef.no/home/MARINTEK/Laboratories/The-Ship-Model-Tank/.

Michailides, C., Gao, Z., Moan, T., 2015. Experimental and numerical study of the response of the offshore combined wind/wave energy concept SFC in extreme environmental conditions. Submitted to Marine Structures.

Michailides, C., Gao, Z., Moan, T., 2016. Experimental Study of the Functionality of a Semisubmersible Wind Turbine Combined with Flap Type Wave Energy Converters. Renewable Energy, 93, 675-690.

Michailides, C., Luan, C., Gao, Z., Moan, T., 2014. Effect of Flap Type Wave Energy Converters on the Response of a Semi-Submersible Wind Turbine in Operational Conditions, 33rd International Conference on Ocean, Offshore and Arctic Engineering, San Francisco, USA.

Muliawan, M.J., Karimirad, M., Gao, Z., Moan, T., 2013. Extreme responses of a combined spar-type floating wind turbine and floating wave energy converter (STC) system with survival modes. Ocean Engineering, 65, 71-82.

Naess, A., Moan, T., 2013. Stochastic dynamics of marine structures. Cambridge University Press.

Sarpkaya, T., 1986. Force on a circular cylinder in viscous oscillatory flow at low Keulegan-Carpenter numbers. Journal of Fluid Mechanics, 165, 61-71.

Sojo, M., Auer, G., 2014. Marine Renewable Integrated Application (MARINA) Platform, Deliverable D1.12, Final Summary Report.

Wan, L., Gao, Z., Moan, T., 2014. Model test of the STC concept in survival modes, 33rd International Conference on Ocean, Offshore and Arctic Engineering. ASME, San Francisco, USA.

Wan, L., Gao, Z., Moan, T., 2015. Experimental and numerical study of hydrodynamic responses of a combined wind and wave energy converter concept in survival modes. Coastal Engineering, 104, 151-169.

Wan, L., Gao, Z., Moan, T., Lugni, C., 2016a. Experimental and numerical comparisons of hydrodynamic responses for a combined wind and wave energy converter concept under operational conditions. Renewable Energy, 93, 87-100.

Wan, L., Greco, M., Lugni, C., Gao, Z., Moan, T., 2016b. Nonlinear motion simulations of a combined wind and wave energy converter concept in survival conditions considering water-entry and exit phenomena. Proceedings of 3rd International Conference on Violent Flows (VF-2016), Osaka, Japan.

Wang, C.-Y., 1968. On high-frequency oscillatory viscous flows. Journal of Fluid Mechanics 32 (01), 55-68.

Wei, Y.W., Rafiee, A., Henry, A., Dias, F., 2015, Wave interaction with an oscillating wave surge converter, Part I: Viscous effects, Ocean Engineering, 104, 185-203.

Wei, Y.W., Abadie, T., Henry, A., Dias, F., 2016, Wave interaction with an oscillating wave surge converter, Part II: Slamming, Ocean Engineering, 113, 319-334.